Internal and external surface characterisation of templating processes for ordered mesoporous silicas and carbons

Matthew R. Hill,[a] Steven J. Pas,[ab] Stephen T. Mudie,[ac] Danielle F. Kennedy[d] and Anita J. Hill[a]

Received 6th October 2008, Accepted 15th January 2009
First published as an Advance Article on the web 18th February 2009
DOI: 10.1039/b817457a

Characterisation of the multiple pore sizes, or heirarchical porosity, within periodic mesoporous silicas, carbons and carbon silica composites using a combination of standard analysis techniques and also positron annihilation lifetime spectroscopy is reported. The PALS technique was found to complement more standard methods of porous materials characterisation such as nitrogen sorption, small angle X-ray diffraction (SAXRD), and thermogravimetric analysis (TGA). Additional information, particularly on the location of polymer within silica materials, and also on internal surfaces, regardless of surface connectivity or long range order was revealed. The templating process was investigated for the widely employed materials SBA-15, KIT-6 and MCF-2.5. Samples were taken at various times throughout the nanotemplating process. Using commonly reported procedures parent templated silicas, ordered mesoporous carbons, their carbon-silica composite materials and second generation silicas were obtained and have been characterised using the suite of techniques. As a result, new information on the development of pore structure derived from the effectiveness of the templating process is reported. The results obtained highlight the factors that influence the process of pore filling. The new details uncovered regarding the porosity of many materials should be useful in the development of further applications with the characterisation serving as a ready reference for future materials development in this field.

Introduction

The preparation of mesoporous materials typically involves the use of a template with a geometry inverse to that desired in the product. Templates are classed as either 'soft' templates, for example surfactants or block copolymers in solution, or 'hard' templates, materials that include porous silicas and carbons.[1,2] The void spaces of the template are filled with a chemical precursor (liquid or gas) that is then consolidated to form the product. Subsequently, the template is removed by either combustion or dissolution.

An important processing issue for the templating of ordered mesoporous materials is the faithful replication of the nanostructured template employed, otherwise known as the intimacy of structural replication. "Hard' templates, such as silicas, may only have their pores partly filled before the material being templated condenses externally to the mesoporous scaffold. During nanocasting, the amount of pore filling possible varies according to both the deposition method employed and the infiltrate material. For example, in the synthesis of mesoporous carbons, pore filling levels are generally no higher than *ca.* 60%, and as a result faithful replication of template nanostructure is not always achieved.[3,4]

Over the last decade there has been an expansion in the number of known ordered mesoporous silicas and their inverse carbon replicates.[5,6] Amongst the discoveries, the control of the symmetry, pore size, and microporosity of these materials has been developed through the fine tuning of synthetic conditions.[7–12]

One important mesoporous silica is the large pore hexagonal SBA-15 (Santa Barbara amorphous)[13,14] Since its first report there has been strong interest in defining its detailed pore structure. It has been found that the size of the mesopores may be controlled through the variation of the synthetic conditions employed. Also detailed argon sorption investigations suggest that micropores give connectivity between the hexagonal mesopores.[15,16] The number and connectivity of these micropores have been shown to be controllable through the change of aging temperature, which varies the degree of hydration present within the polymer template.[15,17] Similar results have been obtained through inhibition of micropore formation *via* the use of inorganic salts.[17]

In 2003, the large pore cubic silica KIT-6 (Korean Institute of Technology) was reported.[18,19] KIT-6 was found to have $Ia\bar{3}d$ symmetry and enantiomeric pairs of interpenetrating channels, providing 3-D connectivity and hence good guest molecule access.[18,19] This work highlighted the ability to alter symmetry with additives. The additives affect the levels of hydration within the structure directing polymer phases. KIT-6 proved to be a 3-D analogue of SBA-15, possessing a 'plumber's nightmare' 3-D interconnecting pore network.[19] Recently this material has found uses in chromatography,[20] the templating of

[a]*CSIRO Division of Materials Science and Engineering, Private Bag 33, Clayton South MDC, Victoria, 3169, Australia*
[b]*Department of Materials Engineering, Monash University, Clayton, Victoria, 3800, Australia*
[c]*Australian Synchrotron, 800 Blackburn Rd, Clayton, Victoria, 3168, Australia*
[d]*CSIRO Division of Molecular and Health Technologies, Private Bag 10, Clayton South MDC, Victoria, 3169, Australia*

mesoporous metal oxides,[21] and the formation of novel battery electrodes.[22]

A third class of mesoporous materials with ultralarge mesopores is known as MCF (mesocellular foam), first reported in 1999.[23] These materials are described as a series of 3-D spherical cages connected by window like openings between adjacent cells. MCF silicas are of particular interest for use in biological applications, stemming largely from the ability to systematically enlarge the connecting windows to a point where large biomolecules may be filtered through the porous network.[24]

In general it is difficult to gain information on the templating process by conventional means since both the internal and external pore surfaces must be monitored to gain a complete understanding of the templating process. In many cases internal surfaces show no connectivity to the surfaces, rendering them inaccessible to many techniques.

In this work we introduce positron annihilation lifetime spectroscopy (PALS) for probing the pore size distribution of mesoporous silicas with large pores. PALS has been employed to some extent on mesoporous silicas,[25–30] including more detailed characterisation of microporosity within SBA-3[31] and the MCM family of silicas.[32–37] However, with careful control of experimental conditions, it is also useful for characterisation of mesopores.

When combined with other techniques and also systematic treatment of samples, PALS is particularly powerful for uncovering the chemical processes prevalent within a class of materials.[38] The PALS experiment measures the lifetimes of positrons, the antiparticles of electrons, by detecting start quanta of 1.28 MeV associated with their birth, and stop quanta of 0.51 MeV associated with their death. Inside the sample, positrons may form *ortho*-positronium (*o*-Ps), which in microporous and mesoporous materials is used to probe porosity, surface area and pore size distributions (PSDs).[39] To date the detection of mesopores with positron annihilation has been only achieved in low concentrations,[32] with most long lifetime components resulting from intergrain spaces.[31] We have found that analyses conducted under ultra-high vacuum (UHV) conditions greatly improve the annihilation in mesopores, resulting in the detection of large mesopores as high as 19.1% of the total porosity in the sample, due to the removal of interfering gases from the pores.

With the goal to obtain a better understanding of the templating process of 'nanocasting', this work demonstrates a detailed study of the commonly reported templating processes associated with three well known ordered mesoporous silica materials: SBA-15, KIT-6 and MCF-2.5. Specifically, the formation of carbons from these 'hard' silica templates by both solution and vapour phase routes, and the subsequent regeneration of mesoporous silicas, have been followed using a combination of BET, TGA, PALS and SAXRD, as shown in Fig. 1. This complementary cache of characterisation techniques can elucidate the structural detail within composite materials, the resultant products and in addition gives a 'snapshot' of the templating process in action.

Experimental

A series of mesoporous silicas and carbons were synthesised, as shown above in Fig. 1. The complete nanocasting cycle was examined, through to the return to mesoporous silicas. Samples are designated as *silica type–casting method–product type.* Silica type: SBA = Santa Barbara amorphous; KIT = Korean Institute of Technology; MCF = mesocellular foam. Casting method: S = solution; V = vapour. Product type: CRB = carbon; CMP = carbon-silica composite; SIL = silica; EtOH = ethanol extracted sample; P123 = sample with pores filled by Pluronic 123.

Materials synthesis

For the production of the pure carbon samples, the silica was removed using 2 × 100 mL (24 hr soaking time per cycle) of 10 % v/v HF solution in 20% v/v EtOH. Prepared carbons proved too hydrophobic for aqueous solutions, preventing complete wetting and hence silica dissolution. HF is a highly hazardous substance and should be handled according to appropriate safety procedures. TGA analysis was performed in all instances to confirm the successful removal of the silica template.

Preparation of SBA-15 silica (SBA-SIL)

SBA-SIL was prepared analogously to that reported by Zhao *et al.*[14] 10.00 g of Pluronic P123 block copolymer was added to 275 mL of 1.6 M HCl. After approximately 4 hours, all of the copolymer appeared to have dissolved. The temperature of the solution was increased to 35 °C and tetraethyl orthosilicate (21.25 g, 0.102 mol) was subsequently added to the solution. The mixture was stirred for a further 20 hours, during which time the solution took on the appearance of an emulsion. The mixture was then transferred to a polypropylene flask and aged without stirring for 24 hours at 100 °C. The resulting precipitate was filtered while hot, air dried at room temperature, and subsequently heated to 500 °C at a rate of 1 °C/min and maintained at this temperature for 6 hours. Yield 6.10 g, 98%.

Solution phase carbonization using SBA silica template (CMK-3)

A previously reported solution based method using sucrose as the carbon precursor was adapted according to the pore volume of the silica employed.[40] To 1.42 g of SBA-15, 1.81 g sucrose in a solution of 0.198 g H_2SO_4 and 7.1 mL water was added. The mixture was vigorously agitated to ensure complete infiltration of the silica by the solution, and then placed in an oven at 100 °C for 6 hours, and then a further 6 hours at 150 °C. The cycle was repeated using 1.16 g sucrose, 0.123 g H_2SO_4 and 7.1 mL water in order to more completely fill the pores. The dark brown powder was then carbonized by heating at 0.5 °C/min to 250 °C, 1 °C/min to 700 °C and maintained at this temperature for four hours. The treatment produced a carbon/silica composite material as a black powder in 2.18 g yield; a percentage value not being applicable due to the indeterminate breakdown mechanism of the sucrose precursor. For the production of the pure carbon samples, the silica was removed using 2 × 100 mL of 10% HF solution.

Preparation of MCF silica (MCF-SIL)

Pluronic P123 (4.00 g, 8.00×10^{-4} mol) was dissolved in HCl (1.6 M, 150 mL) through stirring overnight. Following this, trimethylbenzene (10.00 g, 8.26×10^{-2} mol, 2.5 weight ratio with P123)

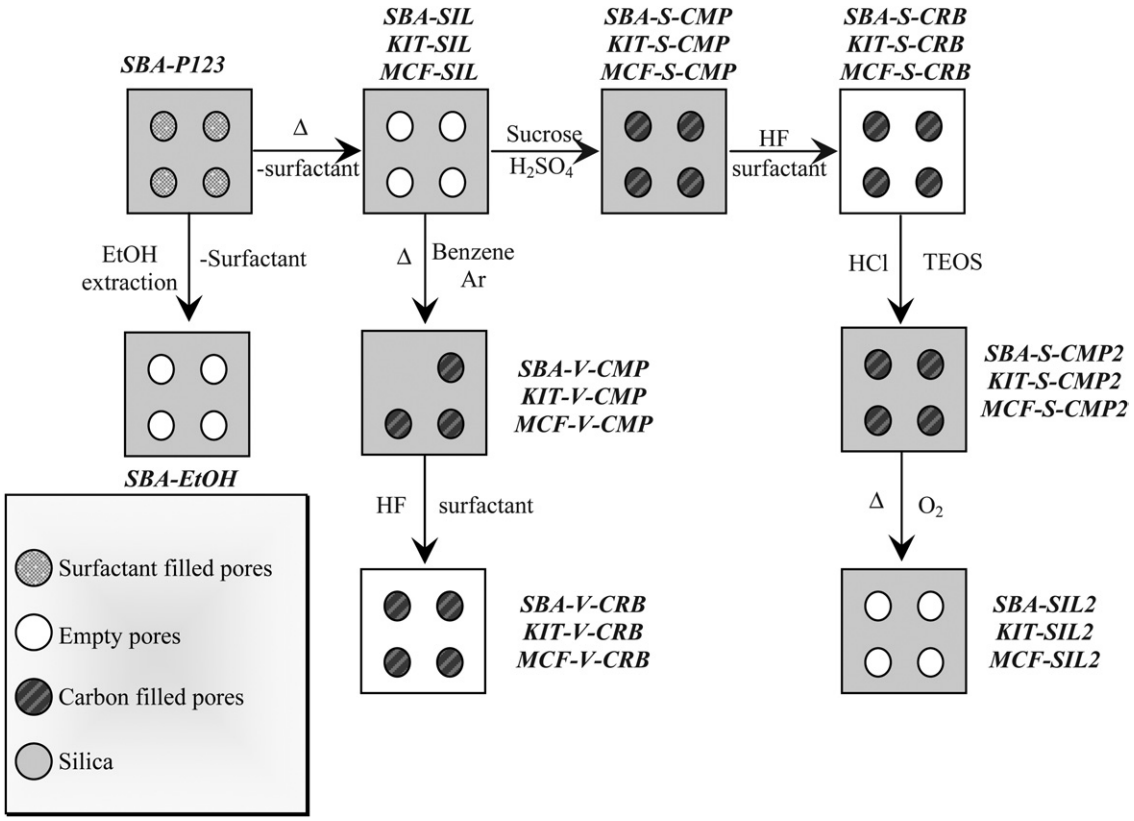

Fig. 1 Schematic showing the relationship between the materials synthesized for the study.

was added and allowed to stir at 38 °C for approximately 60 minutes, taking on the appearance of an emulsion.[41] Tetraethyl orthosilicate (8.80 g, 4.2×10^{-2} mol) was then added and the stirring continued for a further 20 hours. The mixture was then aged without stirring in a polypropylene container at 100 °C for 24 hours, filtered while hot, dried in flowing air, and then calcined at 500 °C for 6 hours, this temperature being approached at a ramp rate of 1 °C/min. Yield 2.45 g, 97%.

Preparation of KIT-6 silica (KIT-SIL)

This material was prepared according to a previously reported procedure.[19] 24.00 g of Pluronic P123 was dissolved at 37 °C in a polypropylene flask containing a mixture of 864 mL water and 47.4 mL of 35% HCl. After complete dissolution 24.00 g of *n*-BuOH was added and the mixture stirred at 37 °C for a further 60 minutes. Subsequently tetraethyl orthosilicate (51.60 g, 0.248 mol) was added and the mixture stirred for a further 20 hours. Stirring was ceased and the mixture was aged at 100 °C for 24 hours. The mixture was filtered while hot, dried under flowing air, washed with a small amount of 10% HCl-EtOH, dried once more, and then calcined at 550 °C for 6 hours, the temperature was ramped at a rate of 1 °C/min. Yield 14.59 g, 98%.

General method for the preparation of carbon casts of silica template using solution phase carbonization (X-S-CRB)

Sucrose was used as the carbon precursor adapting the method of Jun *et al.* according to the pore volume of the silica sample employed.[40] For example: to 1.42 g of SBA-15 with a pore volume of 0.799 cm^3g^{-1}, 1.81 g sucrose in a solution of 0.198 g H_2SO_4 and 7.1 mL water was added. The mixture was vigorously agitated to ensure complete infiltration of the silica pores by the solution, and then placed in an oven at 100 °C for 6 hours, and then 6 hours at 150 °C. The cycle was repeated using 1.16 g sucrose, 0.123 g H_2SO_4 and 7.1 mL water in order to more completely fill the pores. The dark brown powder was then carbonized by heating at 0.5 °C/min to 250 °C, 1 °C/min^{-1} to 700 °C and maintained at this temperature for 4 hours. A carbon/silica composite material was obtained as a black powder in 2.18 g yield; a percentage value is not applicable due to the unknown breakdown mechanism of the sucrose precursor.

For the production of the pure carbon samples, the silica was removed using 2 × 100 mL of 10 % HF solution (24 hr soaking time per cycle) of 10% v/v HF solution in 20% v/v EtOH.

General method for the preparation of carbon casts from silica templates using vapour phase carbonization (X-V-CRB)

Carbon materials were also prepared through the adaptation of previously reported vapour deposition methods.[3,42,43] Approximately 1 g of each silica was placed within a quartz tube furnace under an Ar atmosphere saturated with benzene vapour. Oxygen was flushed from the system using an isothermal step at 100 °C for 2 hours, after which the sample was heated at a rate of 20 °C/min to a temperature of 950 °C, being maintained at this temperature for a further six hours to ensure the maximum amount of carbon incorporation. The furnace was then cooled

to room temperature to yield grey-black materials. Percentage yields are not applicable in these cases due to the use of excess carbon precursor. Relative pore fillings obtained from TGA are more instructive. Silica was removed in a manner identical to that for solution phase analogues.

General method for silica incorporation into ordered mesoporous carbons (X-Y-CRB → X-SIL)

Silica was incorporated into the pores of mesoporous carbon derivatives through the adaptation of a method described by Lu *et al.*[45] For solution prepared silica derived carbons (X-S-CRB) the amount of silica precursor employed was adjusted according to the calculated internal pore volumes of each of the corresponding parent silica with the aim of achieving 60% pore filling across three infiltration cycles. For example: SBA-SIL has a pore volume of 0.799 cm^3g^{-1}. To vigorously stirring SBA-S-CRB (0.3 g) 0.369 g of tetraethyl orthosilicate was added dropwise, followed by 2 drops of 0.1 M HCl. The mixture was then stirred at 40 °C for 3 hours and at 80 °C for a further 3 hours. This process was repeated for a further two cycles. Finally, the black powder was heated to 700 °C under flowing nitrogen with a heating rate of 1 °C/min and maintained at this temperature for 4 hours. The carbon templates were removed from the silicas by heating in air to 550 °C for five hours with a heating rate of 1 °C/min.

Materials characterisation

Nitrogen adsorption experiments were performed on a Quantachrome Autosorb 1 at −196 °C over the partial pressure range $0.005 \leq P/P_o \leq 0.975$. Prior to analysis, samples were degassed at 200 °C and 5×10^{-3} Torr for 24 hours. Parameters including BET surface area, total pore volume, BJH pore size distribution[46] and t-plot micropore analysis were determined using the 'Autosorb 1 for Windows' ver. 1.55 Software, © 2001. BdB-BHH pore size distributions were determined following the procedure described by Lukens *et al.*[47] PALS experiments were performed using an EG&G Ortec fast-fast coincidence system with fast plastic scintillators and a resolution function of 260 ps FWHM (^{60}Co source with the energy windows set to ^{22}Na events). Due to the long lifetimes, and the low counting rate, the coincidence unit was removed and the range of the TAC extended to 200 ns. The powdered samples were packed (>1.5 mm depth) on either side of a 30 μCi ^{22}NaCl foil (2.54 μm Ti foil) source and measured at ~5×10^{-7} Torr. At least five spectra of 4.5 million integrated counts were collected with each spectrum taking about 4.6 h to collect. Data analysis was performed using LT9.[47] The spectra were best fitted with five components with the shortest lifetime fixed to 125 ps, characteristic of *p*-Ps annihilation. For the long lifetimes obtained, the Tao–Eldrup model[49,50] traditionally used for calculating mean pore sizes from mean *o*-Ps lifetimes is not valid; therefore, the mean free path (nm) of the pores was calculated using the rectangular Tao–Eldrup (RTE) model.[51]

The SAXRD system employed was developed by Osmic Inc. (Rigaku Group). This camera uses a CuKα (λ = 1.5408 Å) microfocus source, with a graded multilayer optic to increase flux and monochromate the X-ray beam. For these experiments the camera was configured with a three pinhole geometry for beam collimation, giving a spot size of approximately 0.6 mm FW 10% at the sample position. Throughout the experiments the sample chamber was at atmospheric pressure, however, in order to minimize air scatter a cone shaped attachment extended the post-sample flight tube into the sample chamber, thus reducing the air path length to approximately 3 cm. Beryllium windows separated the evacuated collimation and post-sample flight tubes from the sample environment. A computer controlled *x*-*y* translation stage, mounted inside the sample chamber, was used for sample alignment, with a small photonic science CCD acting as a beam monitor. Fujifilm imaging plates (BAS-MS) and scanner (BAS 5000) were used to collect and readout the SAXS patterns. The imaging plates were mounted in vacuum during exposure, with sample to imaging plate distance approximately 1.6 m. The effective *q*-range of this system is 0.009 $Å^{-1}$ to 0.27 $Å^{-1}$. A silver behenate standard was used to calibrate the reciprocal space vector. Exposure times varied depending on the specific sample, however, in most cases they approached 1 hour. The MCF samples required two exposures (3 minutes and 60 minutes) in order to collect the high dynamic range data. Data reduction (calibration and integration) was achieved using the SAXS15ID[52] software package. Analysis was achieved using the Irena 2 and NIST SAXS Macros for Wavemetrics Igor Pro, as well as custom code written in house using the Interactive Data Language by ITT Visual Information Solutions. TGA measurements were performed in flowing air at a rate of 20mL.min^{-1} in a Pt pan, on a Perkin-Elmer Pyris 1 Analyzer in the range of 20–700 °C with a heating rate of 10 °C/min and an additional isothermal component at 700 °C for 60 minutes.

Results and discussion

The process for nanocasting ordered mesoporous silicas SBA-15, KIT-6 and MCF-2.5 was systematically investigated through the preparation of a series of materials: silica templates (SIL); their carbon casts (CRB), carbon-silica composites (CMP), and second generation silica materials (SIL2), Fig. 1. Traditional analysis techniques, coupled with PALS, have been used to investigate the mesoporous and microporous structures of the silicas, carbons and composite materials produced.

Structural features of silicas

The structural features of the silicas, Fig. 1, generated through soft and hard templating were investigated by a variety of techniques: BET, TGA, PALS and SAXRD.

The PALS technique identifies the heirarchical porosity of the material. The PALS data (Table 1 and Fig. 2) illustrate the multiple scales of porosity readily detectable with positrons. For these materials, τ_3 provides information on molecular scale microporosity in the amorphous silica network ($l = 2$–4 Å), τ_4 is associated with bridging micropore elements ($l \cong 1$ nm) that connect mesopores, and τ_5 gives information on the mesopores ($l = 5$–20 nm), see Fig. 5 for illustration. The hierarchical length scale of the porosity is readily apparent from the *o*-Ps lifetime data. The relative concentration of each type of pore is reflected in the *o*-Ps intensity parameter.

From the PALS analysis the majority of silica samples contain more molecular scale micropores (I_3) than bridging micropores

Table 1 Summary of PALS data for all materials studied. *o*-Ps lifetimes (τ_n), corresponding mean free path of pore length (*l*) and corresponding intensity (I). Calculated standard deviations are in parentheses

	τ_3 (ns)	*l* (nm)	τ_4 (ns)	*l* (nm)	τ_5 (ns)	*l* (nm)	I_3 (%)	I_4 (%)	I_5 (%)
SBA-P123	2.74 (0.02)	0.481 (0.002)	25 (1.5)	1.49 (0.06)	—	—	14.45 (0.10)	3.72 (0.11)	—
SBA-EtOH	1.29 (0.11)	0.310 (0.001)	4.22 (0.17)	0.61 (0.01)	127 (1.8)	32.8 (5.6)	2.36 (0.11)	1.76 (0.04)	12.44 (0.23)
SBA-SIL	0.75 (0.01)	0.164 (0.002)	10.0 (0.65)	0.93 (0.03)	106 (2.7)	11.2 (1.2)	15.52 (0.14)	1.21 (0.01)	16.04 (0.44)
KIT-SIL	0.76 (0.01)	0.169 (0.002)	11.63 (0.80)	1.00 (0.03)	106 (2.2)	11.2 (0.9)	21.95 (0.18)	1.00 (0.03)	19.10 (0.39)
MCF-SIL	0.82 (0.03)	0.185 (0.008)	7.74 (0.18)	0.82 (0.01)	116 (1.4)	16.8 (1.3)	8.13 (0.23)	1.20 (0.02)	16.74 (0.20)
SBA-S-CMP2	2.17 (0.23)	0.42 (0.03)	9.82 (0.86)	0.92 (0.04)	—	—	2.76 (0.12)	2.03 (0.08)	—
KIT-S-CMP2	—	—	—	—	—	—	—	—	—
MCF-S-CMP2	2.16 (0.23)	0.42 (0.03)	10.93 (0.93)	0.97 (0.04)	—	—	2.47 (0.12)	3.17 (0.09)	—
KIT-S-SIL2	0.96 (0.05)	0.22 (0.01)	8.50 (0.34)	0.86 (0.02)	121 (1.6)	21.3 (2.0)	6.11 (0.17)	1.48 (0.04)	14.71 (0.13)
MCF-S-SIL2	2.14 (0.05)	0.415 (0.006)	9.33 (0.16)	0.90 (0.01)	82 (1.7)	5.50 (0.24)	8.09(0.01)	7.15 (0.06)	9.97 (0.17)

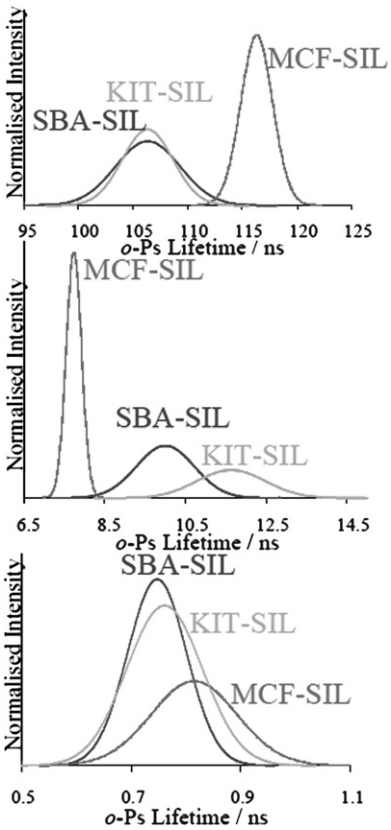

Fig. 2 Pore size distributions derived from PALS data. τ_3 (bottom), τ_4 (middle), τ_5 (top).

(I_4). These molecular scale elements are not connected to the surface and hence cannot be detected by nitrogen adsorption. Micropore volumes can be calculated by t-plot analysis on nitrogen adsorption isotherms for N_2 accessible pores below 2 nm in size. Comparison can also be made between the internal and external micropores with connectivity (t-plot) and the total micropore fraction (PALS: I_3, I_4). PALS and t-plot analysis confirm that KIT-SIL possessed the greatest concentration of micropores (KIT > SBA > MCF).

Microporosity in mesoporous silicas is well known.[10] The microporosity in SBA-SIL has been assigned by Ryoo *et al.* to bridging units between hexagonally aligned mesopore channels.[53] Conversion of the PALS lifetime component to a characteristic mean free path length *l* (which would represent diameter if the pore were spherical) indicates these pores are of the order of 0.93 nm, larger than the pores seen by Ueno *et al.*,[29] who aged their precursor solution at a lower temperature. A pore size of 0.93 ns is, however, in good agreement with the structural features elucidated by Ryoo *et al.*[52] using nitrogen adsorption and TEM. Microporosity in MCF-SIL is likely to be derived from multiple sources. Firstly, due to spherical cage packing in the silica, micropores are generated which have no surface connectivity.[53] Additionally, microporosity stems from the window size that adjoins the adjacent spherical cells.[25]

With regard to the PALS τ_3 measurements, noteworthy is the relative disorder of MCF-SIL. An increased positron lifetime was observed for MCF-SIL (0.82 ns), in comparison to SBA-SIL (0.75 ns) and KIT-SIL (0.76 ns), Fig. 2. As all materials were similarly calcined, it can be concluded that MCF-SIL possesses larger micropores as a result of the templating conditions. This is most likely due to the swelling agent, trimethylbenzene, that is not used in KIT or SBA syntheses and also because KIT and SBA silicas are prepared from more ordered templates. Whilst trimethylbenzene is unlikely to directly enter the walls of the silica to cause this effect, it is possible that it acts *via* indirect means—the swelling of the hydrophobic portion of the template which delivers a larger mesopore may result in the formation of a lower density silica around this pore, hence creating molecular scale free volume elements.

Mesopores are not always detected using PALS as some samples are too conductive to allow the formation of the *o*-Ps probe species. In the samples where mesopores are detected by PALS, they are more abundant than molecular scale micropores, as witnessed by the larger PALS intensity parameters. The results obtained (Table 1) indicate that the largest pores are found in MCF-SIL (116 ns), with no difference in mesopore diameter being observed between KIT-SIL and SBA-SIL (106 ns). However, KIT-SIL shows the highest relative levels of mesopore concentration (I_4) compared to the other pore hierarchies observed in each silica. This demonstrates the difference in mesopore size distribution between KIT-SIL and SBA-SIL, as shown in Fig. 2. Fig. 2 also highlights the distribution of pore sizes witnessed by PALS. One of the contributing factors to peak broadening may be surface roughness, especially in the case of the mesopore lifetimes, τ_5. However, in the case of the MCF series, a direct analysis of surface roughness features was not a major focus of this study.

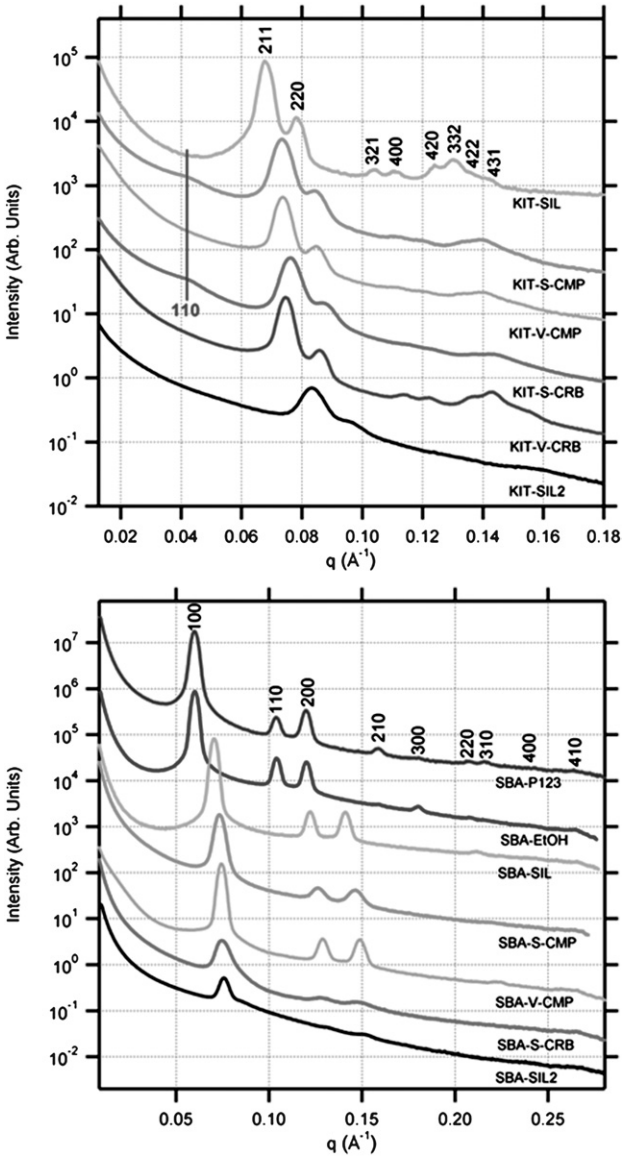

Fig. 3 Stackplot of SAXS patterns for KIT series (top) and SBA series (bottom).

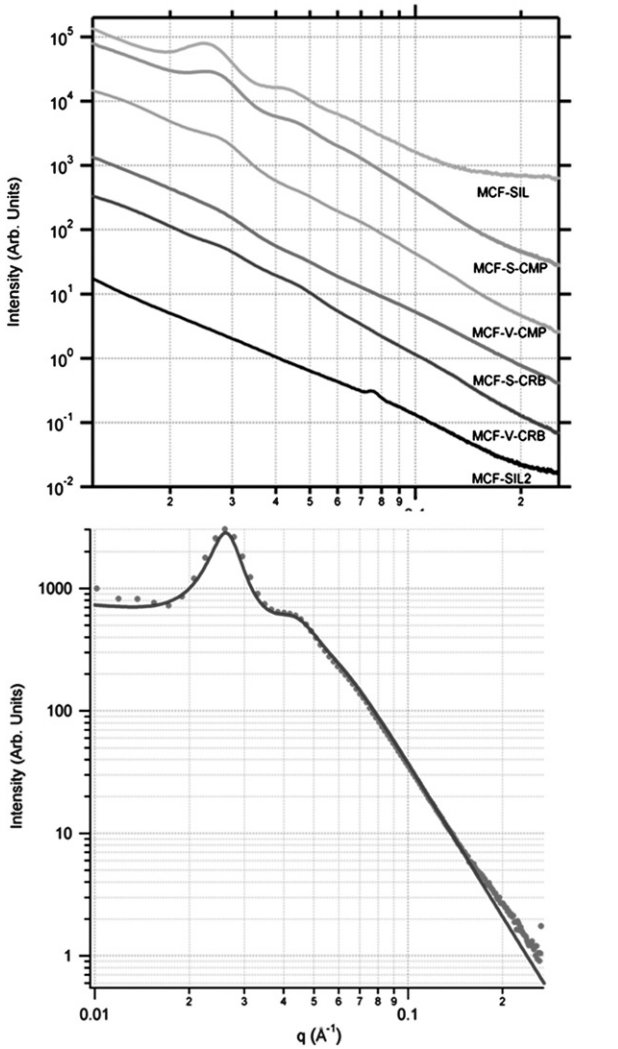

Fig. 4 Stackplot of SAXS patterns for MCF series and fitting of MCF-S-CMP using hard sphere interactions. Circles, experimental data; line, fit.

As shown in Fig. 3, the small angle X-ray data clearly demonstrate the various symmetries of these silicas. Both SBA-SIL and KIT-SIL show diffraction peaks consistent with the anticipated ordering of these materials, *i.e.*, 2D hexagonal for SBA-SIL and $Ia\bar{3}d$ (cubic) for KIT-SIL. The lattice parameters determined from the diffraction peak positions give the pore-to-pore distance: 10.3 nm for SBA-SIL and 22.7 nm for KIT-SIL. The peak intensities may be readily used in a *qualitative* way to make relative judgments of the degree of long range ordering, etc., given suitable pore wall-to-diameter ratios.[41]

Diffraction peaks were not observed for MCF-SIL (Fig. 4, top) indicating that there is no long range order; however, oscillations in the SAXS profile indicate some form of short range ordering. This is not unexpected for this system, with the high pore fraction a driver for local ordering. An attempt at fitting the MCF-SIL data is also shown in Fig. 4 (bottom). Whilst this may be an indicator of diminished long range order, it is also possible that the pore wall-to-diameter ratio could lead to similar effects. However, in the case of the MCF series, the absence of diffraction peaks also points to an absence of long range order.[41]

The experimental data have had a background function subtracted (in a manner similar to that described by Schmidt-Winkel *et al.*[42]), and was then fitted assuming hard-sphere interactions. Unlike Schmidt-Winkel *et al.*[42] a good fit was only achieved with large polydispersity (0.19). The pore fraction was *ca.* 80%. This model gives a reasonable estimate of the pore-to-pore distance.

Formation processes of SBA silica

There are pore hierarchies within all of the SBA-silicas, Fig. 5. Three distinct porous components are present in each material and clear trends were observed between materials generated by different processes. Comparing the abundance of the porous components between silicas provides information on the formation process of the SBA silica in particular.

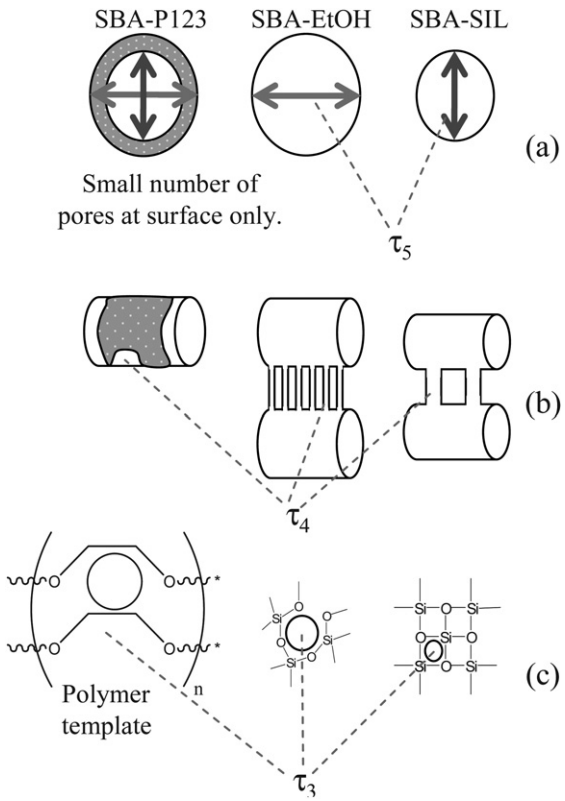

Fig. 5 Schematic outlining the structure and formation of SBA silicas. a: mesopores, b: bridging micropores, c: molecular scale free volume elements.

Table 2 Summary of gas adsorption analyses and unit cell measurements

Sample	S_{BET} $(m^2g^{-1})^a$	Pore volume $(cm^3g^{-1})^b$	Micropore volume $(cm^3g^{-1})^c$	Unit cell parameter $(nm)^d$
SBA-SIL	1050	0.799	0.0410	10.29
SBA-P123	138	0.269	0	12.10
SBA-EtOH	975	1.400	0.108	12.08
SBA-S-CMP	183	0.154	0.0490	9.87
SBA-S-CRB	719	0.809	0	9.74
SBA-S-CMP2	363	0.332	0.0831	—
SBA-S-SIL2	816	1.460	0	9.55
MCF-SIL	582	1.757	0.0850	N/A
MCF-S-CMP	459	0.535	0.167	N/A
MCF-S-CRB	703	0.878	0.128	N/A
MCF-V-CMP	110	0.235	0.00410	N/A
MCF-V-CRB	295	0.631	0	N/A
MCF-S-CMP2	552	0.585	0.171	N/A
MCF-S-SIL2	1179	2.396		N/A
KIT-SIL	823	1.050	0.114	22.66
KIT-S-CMP	439	0.378	0.121	20.94
KIT-S-CRB	604	0.901	0	20.32
KIT-V-CMP	67	0.077	0.000362	20.86
KIT-V-CRB	475	0.660	0	20.61
KIT-S-CMP2	442	0.423	0.146	—
KIT-S-SIL2	1098	1.88	0	18.5

[a] BET surface area calculated from the nitrogen adsorption isotherm in the range $0.05 \leq P/P_o \leq 0.30$. [b] Calculated from a single point on the BET adsorption isotherm at $P/P_o = 0.95$. [c] Calculated using the t-plot method. [d] Determined from SAXRD measurements.

On the mesoporous scale, the pore size (BdB-FHH, Table 4—see later) of SBA-EtOH is significantly enlarged relative to SBA-SIL (10.1 nm, vs. *ca.* 9.0 nm), which is comparable in size to SBA-P123 (Fig. 5a). This finding is confirmed by PALS, which gave lifetimes of 127 ns (SBA-EtOH) and 106 ns (SBA-SIL).

The relative intensities of *o*-Ps components (Table 1) provide information on the concentration of micropores in comparison to mesopores. These data indicate that in solvent extracted materials, micropores are present in significantly greater quantities (Fig. 5, middle) ($I_4/I_5 = 0.0754$ (SBA-EtOH), 0.141 (SBA-SIL)). Gas adsorption micropore volumes (Table 2) confirm this trend, and show a doubling of total internal volume when solvent extraction was used to remove the P123 rather than combustion. This increase may be understood as the sum of an increase in both mesopore size and micropore concentration.

The effect of synthetic conditions on ordering within the silicas on the molecular scale has not been reported previously. The use of PALS has enabled us to investigate the molecular scale ordering of the silica materials at each stage of the synthetic process. PALS results (τ_3) show that order on the molecular scale increases following removal of template, and increases again following calcination, reaching a previously reported value well known for calcined amorphous silicas.[25] τ_3 Lifetimes for SBA-P123 are most likely attributable to annihilation within the low chain packing density regions of the polymer template. The results also show that the extracted silicas contain larger molecular pore scale concentrations than the calcined silicas studied. The PALS results for extracted silicas suggest possible applications. For example, the larger molecular scale pore concentrations indicate the suitability of the extracted silicas for the incorporation of reactive materials, such as in heterogeneous catalysis. Moreover molecular pores of the scale seen for SBA-EtOH (3.1Å) are known to be very useful for molecular sieving.[55,56]

The analysis of SBA-P123 using a combination of PALS (Table 1) and nitrogen adsorption (Table 2) reveals the location of the dehydrated block copolymer template amongst the formed silica network. Nitrogen adsorption data for SBA-P123 indicates a comparatively low surface area (87% lower that when calcined), absent microporosity (micropores should be completely filled with template), and a pore size similar to the calcined SBA-SIL (*ca.* 7 nm). In addition, the PALS data show no long PALS lifetime component corresponding to this pore size. Combined, these results indicate that most pores are filled with the polymer template, and the remaining mesopores are coated by a thin layer of polymer that delivers a pore size similar to the calcinate SBA-SIL. The low BET surface area confirms the low concentration of these mesopores, placing them below the detection limit of PALS, which becomes less sensitive with increasing pore size. Using the reduced BET surface area as a guide, this lifetime component would be present in only *ca.* 1% intensity, which would not be reliably detected.

The silica materials were also analysed using SAXRD. The SAXRD profiles in Fig. 3 show that the lattice parameters for SBA-P123 and SBA-EtOH are the same. This indicates that the removal of the polymer using ethanol does not cause the silica structure to shrink or expand, and thus we would assume the pore size is identical for the two structures. However, for

SBA-EtOH the higher order diffraction peaks are less intense, or missing, suggesting that the interface between the silica and pore is more diffuse (*e.g.*, roughened) with respect to SBA-P123. The lattice parameter (pore centre-to-pore centre) distance is smaller for SBA-SIL as indicated by the diffraction maxima shifting to higher reciprocal space vector q. This suggests a smaller pore size for the material that is calcined. These observations are consistent with the PALS results which indicated that the silica/polymer composite SBA-P123 possessed the same enlarged mesopore size as SBA-EtOH, with the silica surface of pores close to the surface coated by a thin layer of polymer that rendered these pores of similar size to SBA-SIL according to gas adsorption and which would also generate a smooth pore surface.

The above observations are consistent with the PALS and nitrogen sorption which indicated that the silica/polymer composite SBA-P123 possessed the same enlarged mesopore size as SBA-EtOH, with the silica surface of pores close to the surface coated by a thin layer of polymer that rendered these pores of similar size to SBA-SIL according to gas adsorption.

Regeneration of silicas—completion of the templating process

The process of regenerating mesoporous silica materials from their carbon casts was investigated through the analysis of carbon-silica composites and end-product silicas (denoted as -CMP2 and -SIL2 respectively). The composite materials were generated from carbon casts of parent silicas by the incorporation of the solution based silica precursor, TEOS, in the presence of acid catalyst. Carbon was then removed from the composite materials *via* calcination, delivering the second generation silicas.

TGA analysis of composite materials was performed, Fig. 6. TGA reveals that the composite material with the least amount of carbon and hence the highest level of silica was that derived from the 3D bicontinuous cubic template, KIT-S-CMP. The gas adsorption data summarized in Table 2 indicate that the total internal volume of all composite materials (MCF-CMP2, KIT-CMP2, SBA-CMP2) is much larger in comparison to their original composite counterparts (MCF-CMP, KIT-CMP, SBA-CMP). This is indicative of the lower degree of structural replication evident for these materials, further supported by increased micropore volumes and as determined by t-plot analysis.

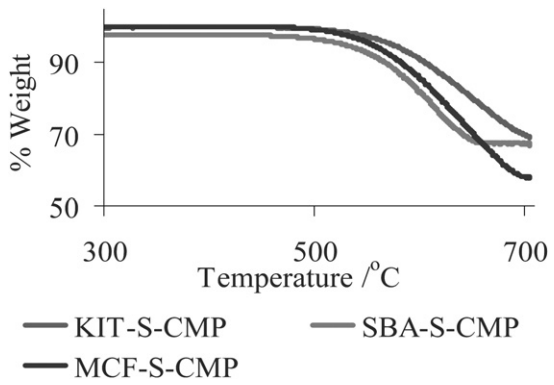

Fig. 6 Thermogravimetric analysis showing the effect of template structure on silica incorporation.

PALS analysis of the composite materials can determine the intimacy of the templating process, as *o*-Ps can only form within insulating environments. Therefore, the presence of the probe species, *o*-Ps, for composite materials may be regarded as a diagnostic for the intimacy of template replication with the formation of *o*-Ps signifying a lack of contact or a gap between silica and carbon. The PALS data (Table 1) show that no *o*-Ps was formed in the accessible 3D bicontinuous cubic sample KIT-CMP2, indicating intimacy between the carbon template and the silica. The intimacy of replication in the case of the KIT silicas is presumably due to the three dimensional connectivity of the pores allowing for intimate surface replication. *o*-Ps was seen in the other composite samples indicating that they were less faithfully templated. Within the less faithfully templated samples (MCF-CMP2 and SBA-CMP2), lifetimes correlating to vacancy sizes of approximately 0.4 nm (τ_3) and 0.95 nm (τ_4) are observed. The τ_3 values observed differ substantially from those observed for molecular level structuring in the original silica samples, being significantly larger. This is indicative of reduced order in the templated samples even at the molecular level. The τ_4 values obtained are indicative of voids left between the silica and carbon surfaces, which are not necessarily connected to the external surface. No extended lifetimes (τ_5, indicative of mesopores) were observed in any of the composite materials, therefore, even the less faithfully templated samples were well templated with no large voids detected.

SAXRD patterns obtained from the analysis of the silica composites clearly demonstrate the disruption of order in these silica composites that occurs during the regeneration process. None of the second generation silicas possess higher order reflections. There is also a clear trend towards higher reciprocal space vector (q) reflections for these regenerated materials, indicating that the pore-to-pore distance has decreased as a result of the processing.

The analysis of the composite materials indicates that the regeneration of silicas through the solution templating process results in an increase in surface areas and pore volumes, but a decrease in pore-to-pore distance. PALS clearly indicates that the silica itself is less compacted at the molecular scale during regeneration and that intimate contact between silica and carbon is not achieved.

Solution and vapour phase template replication

Carbons templated from mesoporous silica templates are strongly influenced by their method of deposition. Carbons were deposited onto SBA, KIT and MCF silica templates by both solution and vapour phase means (see Experimental section) to study the influence of these methods on both the mechanism of pore filling and the properties of the carbons afforded. As seen in Table 3, TGA revealed that vapour phase deposition gave increased levels of pore filling, delivering carbon materials that exhibited enhanced thermal stability in air. Compared to solution deposited composite materials, vapour deposited composites showed greater weight losses in TGA measurements, indicating greater carbon incorporation levels, as high as 92% for the KIT series (Table 3). Vapour deposited carbons are prepared at much higher temperatures (*ca.* 1000 °C), and as a consequence are likely to be more graphitic in nature, accounting for their increased thermal stability.

Table 3 Weight percentage of carbon in composites as determined by TGA, compared to the calculated maximum for 100% pore filling

	SBA-S-CMP	KIT-S-CMP	KIT-V-CMP	MCF-S-CMP	MCF-V-CMP
Theoretical maximum (%)	42.1	48.8	48.8	61.5	61.5
Found (%)	33.2	30.9	40.5	42.3	46.0
Shortfall (%)	8.9	17.9	8.3	19.2	15.5

The increased levels of carbon incorporation in vapour deposited samples are also reflected in the gas adsorption data. Vapour deposited samples (KIT-V-CMP, MCF-V-CMP) possess diminished micropore volume (as measured by gas adsorption) relative to their solution deposited counterparts, with micropores being almost absent in these vapour deposited materials. Observed microporosity (Table 2) in composites may be regarded as an indicator of voids between the template and carbon product, and their absence within vapour deposited samples may point to improved templating with this method. BET analyses also reveal that vapour phase deposition results in diminished surface areas and internal pore volumes, and BdB-FHH analyses show smaller pore sizes for these vapour phase deposited materials. Such findings are consistent with increased levels of carbon in vapour deposited samples.

SAXRD also highlights the structural differences between solution and vapour deposited materials. The mesoporous materials KIT and SBA show higher order reflections for vapour deposited composites that are absent for solution deposited analogues. These higher order reflections are indicative of sharper boundaries between the silica matrix and the carbon. SAXRD also provides information on how the pore filling procedure affects the product structure. As seen in Fig. 3, a forbidden (110) peak is seen for solution derived KIT composite and carbon materials, indicating a disruption to the $Ia\bar{3}d$ symmetry. Most likely this is as a result of asymmetric pore filling for solution derived materials, caused by the removal of solvent and decomposition of the carbon precursor. Note that this disruption in symmetry must have a different origin than that described by Xing *et al.*,[57] because it is observed for the composite material, where the silica support has not yet been removed. The vapour phase composites do not display the (110) peak, indicating that the symmetry has not been modified, which suggests complete filling of the pores.

SAXRD, BET and TGA data suggest that the templating is more intimate *via* the vapour phase than the more common solution phase deposition route. The carbons derived from vapour deposition are more graphitic and hence more stable.

Complementarity of characterisation techniques

A suite of characterisation techniques have been used to analyse silicas at various stages of the nanocasting process. These techniques are on the whole complementary whilst also providing different information. Nitrogen adsorption provides information on pore size, pore volume, and surface area, but its reach is limited to pores that have surface connectivity. SAXRD provides the unit cell dimensions and is most effective for materials with long range order. PALS is effective for internal and external surfaces, regardless of surface connectivity or long range order, but only if the surface area is high enough (>50m^2g^{-1}), and internal surfaces are sufficiently insulating to allow the formation of *o*-Ps. Combining these complementary techniques has allowed a novel surface and pore size analysis of samples throughout the various stages of the templating process.

A comparison of results obtained for pore size determination using the various techniques is tabulated in Table 4. It highlights the varying suitabilities of techniques with regard to the characterisation of specific nanostructural features in samples taken throughout the templating process. As expected, the systematic underestimation of pore size[16,58] from the BJH method[46] is again evident.[47] PALS data gave very useful information on the hierarchical porosity, in particular micropore and molecular scale free volume elements, information not otherwise easily attainable. Table 4 also highlights that PALS is not a suitable technique for mesoporous materials with high carbon content; the materials are too conductive to allow for the formation of the *o*-Ps probe species and hence prevents the characterisation of mesopores using this technique. The conversion of measured *o*-Ps lifetimes to corresponding pore sizes for the large mesopores in these materials is achieved with varying accuracy. Although this conversion has been shown to be accurate for SBA-3 and related microporous silicas, the effectiveness of the lifetime-to-pore-size conversion clearly diminishes at larger pore sizes. Under the rectangular Tao–Eldrup (RTE) model used in this study, which is the most valid model for larger mesopores[51] a small change in lifetime corresponds to a large change in predicted pores sizes at long lifetimes. This is due to the fact that in larger pores, the increased surface radius of curvature begins to resemble a flat surface to the *o*-Ps probe. Relative comparison of PALS lifetimes is therefore a better tool for mesopore characterisation. SAXRD gives good comparative pore sizes to those obtained from BdB-FHH analyses for the ordered SBA-15 series

Table 4 Comparison of pore size analysis techniques

Sample	BJH pore size (nm)	BdB-FHH pore size (nm)	PALS pore size (nm)	SAXRD unit cell (nm)
SBA-SIL	6.89	9.0	0.164, 0.93, 11.2	10.29
SBA-P123	7.0	10.1	0.481, 1.49, —	12.10
SBA-EtOH	8.4	11.6	0.31, 0.61, 32.8	12.08
SBA-S-CMP	6.3	7.4	—	9.87
SBA-S-CRB	—	10.2	—	9.74
SBA-S-CMP2	3.8	4.3	—	—
SBA-S-SIL2	—	—	—	9.55
MCF-SIL	25.0	33.4	0.185, 0.82, 16.8	—
MCF-S-CMP	18.0	30.3	—	—
MCF-S-CRB	—	30.3	—	—
MCF-V-CMP	—	22.7	—	—
MCF-V-CRB	4.0, 20.0	6.3, 29.3	—	—
MCF-S-CMP2	3.5, 20.0	3.5, 28.7	—	—
MCF-S-SIL2	12.0	29.1	5.5	—
KIT-SIL	8.0	10.5	0.169, 1.0, 10.6	22.66
KIT-S-CMP	6.8	9.0	—	20.94
KIT-S-CRB	3.5	5.3	—	20.32
KIT-V-CMP	6.3	9.1	—	20.86
KIT-V-CRB	3.5	5.2	—	20.61
KIT-S-CMP2	2.3	3.7	0.42, 0.97, —	—
KIT-S-SIL2	3.8	6.3	0.42, 0.9, 21.3	18.5

when wall thickness is taken into account. The unit cell for the KIT series is significantly larger than the obtained BdB-FHH values due to its bicontinuous geometry that contributes two mesopore channels to each unit cell.

Conclusions

An integrated understanding of the templating processes associated with the formation of three ordered mesoporous silicas (SBA-15, KIT-6 and MCF-2.5) and related carbons has been achieved. The internal and external structure of samples taken throughout the process were analysed using a suite of techniques including N_2 sorption, SAXRD and TGA. PALS has also been applied to the analysis of mesoporous silicas for the first time.

An analysis of the relative suitability of techniques for pore size determination was undertaken. Small angle X-ray analysis was found to be useful in the determination of porosity, but was more suited to materials with long range order. PALS was particularly useful in the simultaneous measurement of multiple scales of porosity, in particular microporous elements, or those without surface connectivity. Combination of these techniques with more commonly employed gas adsorption and thermogravimetric analysis provided a clear picture of templating within mesoporous silicas.

The relative concentrations of meso- and micro-porosity in the silicas were quantified for the first time using PALS. The highest mesopore concentration was found in KIT-6 silica and the greatest micropore concentration in SBA-15 silica. The template geometry and preparation route were found to affect order or packing of the silica on the molecular scale, with large free volume elements being measured in MCF silicas. The location of the polymer in the templated silica SBA-P123 was able to be determined through a combination of PALS and nitrogen adsorption. It was found that most of the pores were filled with the dehydrated polymer with the remainder of the mesopores coated with a thin film of the polymer resulting in the smaller pores sizes than the silica once the polymer was removed, SBA-EtOH. Removal of polymer template from SBA-P123 *via* extraction with EtOH, as opposed to calcination, resulted in the formation of both larger mesopores and a higher concentration of micropores.

Both vapour phase and solution phase incorporation of carbon into the silica frameworks was utilised. Vapour phase deposition of carbons was found to result in materials with increased thermal stability, improved pore filling, and a lower surface area. SAXRD revealed that these carbons had extended order, which correlates with their thermal stability. Regeneration of silicas from carbon templates highlighted the variability in template-product intimacy, which was readily detected by PALS.

Detailed analysis of the templating process has shown that structural replication is most faithful for the cubic bicontinuous KIT series, presumably due to the three dimensional connectivity of the pores allowing for intimate surface replication.

We have presented a comprehensive overview of the synthesis and characterisation of widely utilised periodic mesoporous materials. The new details uncovered regarding the porosity of many materials should be useful in the development of further applications. The evaluation and comparison of characterisation techniques including the under-utilised PALS should serve as a ready reference for future materials development in this field.

Acknowledgements

The authors thank Mr Tim Harvey for experimental assistance and advice, and the School of Physics, Monash University, for access to the SAXRD instrument. PALS experiments were carried out within the framework of the ARC Centres of Excellence program through the ARC Centre for Electromaterials Science. MRH acknowledges financial support through the CSIRO Hierarchical Materials Emerging Science Initiative. STM acknowledges the Australian Synchrotron Research Program for the provision of a Post-Doctoral Fellowship.

References

1 F. Schuth, *Angew. Chem. Int. Ed.*, 2003, **42**(31), 3604.
2 F. Hoffmann, M. Cornelius, J. Morell and M. Froba, *Angew. Chem. Int. Ed.*, 2006, **45**(20), 3216.
3 Y. D. Xia and R. Mokaya, *Adv. Mater.*, 2004, **16**(11), 886.
4 F. Su, J. Zeng, X. Bao, Y. Yu, J. Y. Lee and X. S. Zhao, *Chem. Mater.*, 2005, **17**(15), 3960.
5 Y. Wan and D. Y. Zhao, *Chem. Rev.*, 2007, **107**(7), 2821.
6 F. Hoffmann, M. Cornelius, J. Morell and M. Froba, *J. Nanosci. Nanotech.*, 2006, **6**(2), 265.
7 H. F. Yang and D. Y. Zhao, *J. Mater. Chem.*, 2005, **15**(12), 1217.
8 R. Ryoo, S. H. Joo, M. Kruk and M. Jaroniec, *Adv. Mater.*, 2001, **13**(9), 677.
9 F. Schuth and F. Marlow, *Nature*, 2007, **449**(7162), 550.
10 A. H. Lu and F. Schuth, *Adv. Mater.*, 2006, **18**(14), 1793.
11 A. H. Lu and F. Schuth, *Comp. Rend. Chim.*, 2005, **8**(3–4), 609.
12 F. Schuth., The evolution of ordered mesoporous materials. In *Mesoporous Crystals and Related Nano-Structured Materials*, Elsevier Science BV, Amsterdam, Netherlands, 2004; Vol. 148, pp 1.
13 D. Y. Zhao, J. L. Feng, Q. S. Huo, N. Melosh, G. H. Fredrickson, B. F. Chmelka and G. D. Stucky, *Science*, 1998, **279**(5350), 548.
14 D. Y. Zhao, Q. S. Huo, J. L. Feng, B. F. Chmelka and G. D. Stucky, *J. Am. Chem. Soc.*, 1998, **120**(24), 6024.
15 M. Kruk, M. Jaroniec, C. H. Ko and R. Ryoo, *Chem. Mater.*, 2000, **12**(7), 1961.
16 M. Kruk, M. Jaroniec and A. Sayari, *Langmuir*, 1997, **13**(23), 6267.
17 A. Sayari and Y. Yang, *Chem. Mater.*, 2005, **17**(24), 6108.
18 F. Kleitz, S. H. Choi and R. Ryoo, *Chem. Commun.*, 2003, (17), 2136.
19 T. W. Kim, F. Kleitz, B. Paul and R. Ryoo, *J. Am. Chem. Soc.*, 2005, **127**(20), 7601.
20 A. Galarneau, J. Lapichella, D. Brunel, F. Fajula, Z. Bayram-Hahn, K. Unger, G. Puy, C. Demesmay and J. L. Rocca, *J. Sep. Sci.*, 2006, **29**(6), 844.
21 A. Rumplecker, F. Kleitz, E. L. Salabas and F. Schuth, *Chem. Mater.*, 2007, **19**(3), 485.
22 J. Y. Luo, J. J. Zhang and Y. Y. Xia, *Chem. Mater.*, 2006, **18**(23), 5618.
23 P. Schmidt-Winkel, W. W. Lukens, D. Y. Zhao, P. D. Yang, B. F. Chmelka and G. D. Stucky, *J. Am. Chem. Soc.*, 1999, **121**(1), 254.
24 Y. J. Han, G. D. Stucky and A. Butler, *J. Am. Chem. Soc.*, 1999, **121**(42), 9897.
25 S. Boskovic, A. J. Hill, T. W. Turney, M. L. Gee, G. W. Stevens and A. J. O'Connor, *Prog. Solid State Chem.*, 2006, **34**(2–4), 67.
26 J. Goworek, J. Wawryszczuk and R. Zaleski, *J. Colloid Interface Sci.*, 2001, **243**(2), 427.
27 Y. J. He, H. Y. Zhang, Y. B. Chen, H. Y. Wang and T. Horiuchi, *J. Phys.: Condens. Matter*, 2001, **13**(11), 2467.
28 K. Ito, Y. Yagi, S. Hirano, M. Miyayama, T. Kudo, A. Kishimoto and Y. Ujihira, *J. Ceram. Soc Jpn.*, 1999, **107**(2), 123.
29 Y. Ueno, A. Tate, O. Niwa, H. S. Zhou, T. Yamada and I. Honma, *Chem. Commun.*, 2004, (6), 746.
30 H. Y. Zhang, Y. J. He, Y. B. Chen and H. Y. Wang, *J. Appl. Phys.*, 2002, **92**(12), 7636.
31 M. Koshimizu, K. Shimokita, H. S. S. Zhou, I. Honma and K. Asai, *J. Phys. Chem. C*, 2008, **112**(24), 8779.
32 R. Zaleski, J. Wawryszczuk and T. Goworek, *Radiat. Phys. Chem.*, 2007, **76**(2), 243.

33 J. Goworek, A. Borowka, R. Zaleski and R. Kusak, *J. Therm. Anal. Calorim.*, 2005, **79**(3), 555.
34 R. Zaleski, J. Wawryszczuk and T. Goworek, *Chem. Phys. Lett.*, 2003, **372**(5–6), 800.
35 R. Zaleski, J. Wawryszczuk, J. Goworek, A. Borowka and T. Goworek, *J. Colloid Interface Sci.*, 2003, **262**(2), 466.
36 R. Zaleski, A. Borowka, J. Wawryszczuk, J. Goworek and T. Goworek, *Chem. Phys. Lett.*, 2003, **372**(5–6), 794.
37 J. Wawryszczuk, J. Goworek, R. Zaleski and T. Goworek, *Langmuir*, 2003, **19**(7), 2599.
38 M. R. Hill, T. J. Bastow, S. Celotto and A. J. Hill, *Chem. Mater.*, 2007, **19**(11), 2877.
39 J. C. Groen, L. A. A. Peffer and J. Perez-Ramirez, *Microporous Mesoporous Mater.*, 2003, **60**(1–3), 1.
40 S. Jun, S. H. Joo, R. Ryoo, M. Kruk, M. Jaroniec, Z. Liu, T. Ohsuna and O. Terasaki, *J. Am. Chem. Soc.*, 2000, **122**(43), 10712.
41 K. Flodstrőm, C. Teixeira, H. Amenitsch, V. Alfredsson and M. Linden, *Langmuir*, 2004, **20**, 4885.
42 P. Schmidt-Winkel, W. W. Lukens, P. D. Yang, D. I. Margolese, J. S. Lettow, J. Y. Ying and G. D. Stucky, *Chem. Mater.*, 2000, **12**(3), 686.
43 Y. D. Xia and R. Mokaya, *Adv. Mater.*, 2004, **16**(17), 1553.
44 Y. D. Xia; Z. X. Yang; R. Mokaya, Synthesis of hollow spherical mesoporous N-doped carbon materials with graphitic framework. In *Nanoporous Materials Iv*, Elsevier Science BV, Amsterdam, Netherlands, 2005; Vol. 156, pp 565.
45 A. H. Lu, W. Schmidt, A. Taguchi, B. Spliethoff, B. Tesche and F. Schuth, *Angew. Chem. Int. Ed.*, 2002, **41**(18), 3489.
46 L. G. Joyner, E. P. Barrett and R. Skold, *J. Am. Chem. Soc.*, 1951, **73**(7), 3155.
47 W. W. Lukens, P. Schmidt-Winkel, D. Y. Zhao, J. L. Feng and G. D. Stucky, *Langmuir*, 1999, **15**(16), 5403.
48 J. Kansy, *Nucl. Instrum. Methods A*, 1996, **374**, 235.
49 S. J. Tao, *J. Chem. Phys*, 1972, **56**, 5499.
50 M. Eldrup, D. Lightbody and J. N. Sherwood, *Chem. Phys*, 1981, **63**, 51.
51 T. L. Dull, W. E. Frieze, D. W. Gidley, J. N. Sun and A. F. Yee, *J. Phys. Chem. B*, 2001, **105**(20), 4657.
52 D. Cookson, N. Kirby, R. Knott, M. Lee and D. Schultz, *J. Synch. Rad.*, 2006, **13**, 440.
53 R. Ryoo, C. H. Ko, M. Kruk, V. Antochshuk and M. Jaroniec, *J. Phys. Chem. B*, 2000, **104**(48), 11465.
54 Y. Oda, K. Fukuyama, K. Nishikawa, S. Namba, H. Yoshitake and T. Tatsumi, *Chem. Mater.*, 2004, **16**(20), 3860.
55 M. C. Duke, S. Mee and J. C. D. da Costa, *Water Res.*, 2007, **41**(17), 3998.
56 G. Q. Lu, J. C. D. da Costa, M. Duke, S. Giessler, R. Socolow, R. H. Williams and T. Kreutz, *J. Colloid Interface Sci.*, 2007, **314**(2), 589.
57 L. H. Xing, J. H. Huang, S. J. Wu, H. S. Wang, K. Song, H. Y. Xu, Z. Q. Wang and Q. B. Kan, *Carbon*, 2007, **45**(1), 220.
58 Jc. Broekhof and J. H. Deboer, *J. Catal.*, 1967, **9**(1), 15.